Badrakh and Albert, 2026. Mongolian Geoscientist 31 (62)
https://doi.org/10.5564/mgs.v31i62.4567

Mongolian Geoscientist

Original Article

Integrated Random Forest-based porphyry copper prospectivity mapping with EnMAP hyperspectral validation in southeastern Mongolia

Munkhsuren Badrakh [1,2*], Gáspár Albert[2]

[1]*Doctoral School of Earth Sciences, Faculty of Science, Eötvös Loránd University, 1117 Budapest, Hungary*
[2]*Institute of Cartography and Geoinformatics, Faculty of Informatics, Eötvös Loránd University, 1117 Budapest, Hungary*

**Corresponding author:* muujuub@student.elte.hu, *ORCID:* 0000-0001-8328-128X

ARTICLE INFO

Article history:

Received 18 November, 2025
Revised 18 February, 2026
Accepted 05 March, 2026

ABSTRACT

Porphyry copper systems in southern Mongolia are important targets for mineral exploration, yet data-driven mineral prospectivity mapping has limited application in this region. In this study, we developed a Random Forest model to evaluate porphyry copper prospectivity and validated the results using independent hyperspectral evidence from the Environmental Mapping and Analysis Program. Despite limited data availability, a 15-layer predictor stack at 250 m resolution was created using geological, structural, topographic, geophysical, and Sentinel-2A-derived spectral indices. The model was trained using 264 balanced samples, including 132 positive samples buffered around 33 confirmed porphyry occurrences to reduce spatial overlap, and 132 negative samples selected using spatial exclusion masks. Two model configurations were tested: Model A, which included intrusion proximity variables, and Model B, which excluded them. Model A achieved an area under the receiver operating characteristic curve of 0.920 and an overall accuracy of 0.837, outperforming Model B, which reached a lower value of 0.745 and an accuracy of 0.714, highlighting the strong metallogenic influence of intrusive bodies. Prospectivity maps and top-decile target zones revealed anomalies that align with known deposits at Tsagaan Suvarga and Bronze Fox, and with prospects at Shuteen and Mandakh, while identifying additional unexplored target areas. Independent validation using Environmental Mapping and Analysis Program-derived alteration maps further demonstrated that top-ranked pixels from Model A overlapped with 22.23% of intense Al-OH alteration, 9.91% of Mg-Fe-OH alteration, and 31.12% when combined, outperforming Model B. These results indicate that combining Random Forest prospectivity mapping with hyperspectral alteration information improves prospectivity assessments for concealed porphyry exploration.

Keywords: Mineral prospectivity mapping (MPM); Machine learning; Hyperspectral remote sensing; Alteration mineral mapping; Porphyry copper systems; Southern Mongolia

INTRODUCTION

Porphyry copper systems are large zones of hydrothermally altered rock centered on porphyry intrusions and are among the most important global sources of copper, molybdenum, and gold (Sillitoe, 2010). These systems usually form in magmatic arc settings along active continental margins associated with subduction zones (Sun et al., 2017). They show extensive hydrothermal alteration zones, including potassic, phyllic, argillic, and propylitic assemblages, which are closely associated with ore mineralization (Lowell and Guilbert, 1970). Copper is typically found in rocks altered by hydrothermal processes related to granitoid porphyry intrusions and nearby wall rocks (Cooke et al., 2005; Sillitoe, 2010).

Porphyry Cu-Au deposits are the main source of copper worldwide and also make a significant contribution to global gold production (Phillips et al., 2023). Since near-surface mineral deposits are running out, exploration is shifting toward the discovery of hidden deposits using advanced technologies (Ponomarenko et al., 2021; Okada, 2022; Ghorbani et al., 2023; Yang et al., 2024; Asadzadeh and Chabrillat, 2025).

Mineral prospectivity mapping (MPM), also known as mineral potential mapping, is a method of identifying areas that may contain mineral deposits by combining various geoscientific datasets in a GIS (Porwal and Kreuzer, 2010). It integrates diverse layers of spatial data to identify and prioritize regions prospective for both known and undiscovered mineralization (Bonham-Carter, 1994; Behnia et al., 2023). MPM approaches are generally classified into knowledge-driven and data-driven (Porwal and Kreuzer, 2010; Carranza and Laborte, 2015). Knowledge-driven methods often use conceptual geological models and expert judgment to subjectively weigh exploration criteria (Ali Hosseini and Abedi, 2015). In contrast, data-driven techniques use statistical or computational models trained on known mineral deposits to quantitatively find links between predictor variables and mineralization (Behnia et al., 2023). Machine learning algorithms (MLAs) like Support Vector Machines, Artificial Neural Networks, and Random Forest (RF) have shown they are effective at modeling complex, nonlinear relationships in multi-source geoscientific data (e.g., Zuo and Carranza, 2011; Abedi et al., 2012; Rodriguez-Galiano et al., 2015; Daoud et al., 2025; Mokhtari et al., 2025; Mastop De Oliveira et al., 2025). Recent research shows that RF is one of the most reliable machine learning methods for MPM because it offers high classification accuracy, resists overfitting, and can manage complex, high-dimensional data (Behnia et al., 2023; Mokhtari et al., 2025; Mastop De Oliveira et al., 2025).

Independent of machine learning applications, hydrothermal alteration in porphyry systems creates unique mineral and spectral signatures observable in remote sensing data. Important alteration minerals have specific absorption features in the visible to near-infrared and shortwave infrared (VNIR-SWIR) regions, which allow their identification with multispectral and hyperspectral sensors (Rowan and Mars, 2003; Hauff, 2008; Mars and Rowan, 2011). The spatial distribution of these minerals provides valuable indicators of hydrothermal zonation and serves as a proxy for concealed porphyry mineralization (Asadzadeh et al., 2024a). The Environmental Mapping and Analysis Program (EnMAP), operated by the German Aerospace Center, is a hyperspectral satellite mission launched in 2022, capturing data across 420-2450 nm in 224 spectral bands with a spatial resolution of 30 m (Guanter et al., 2015; Chabrillat et al., 2024). It provides high-quality, radiometrically calibrated hyperspectral data designed for advanced Earth observation and mineral exploration applications. Recent studies have demonstrated its strong potential for geological and mineral applications. For instance, Asadzadeh et al. (2024c) confirmed the sensor's capability to accurately delineate hydrothermal alteration zonation in porphyry copper systems, while Shebl et al. (2025) validated its effectiveness for detailed lithological and structural mapping in the Arabian Nubian Shield. Additionally, Asadzadeh et al. (2024b) reported the first satellite-based detection of neodymium (Nd) absorption features at the Mountain Pass REE deposit. Most recently, Asadzadeh and Chabrillat (2025) demonstrated EnMAP's versatility in mapping various mineral deposit types, including porphyry Cu-Au, Volcanogenic massive sulfide, Mississippi valley type, and carbonatite systems, highlighting its global potential for mineral exploration.

Southern Mongolia hosts several known porphyry copper deposits (Batkhishig et al., 2014) and remains highly prospective for undiscovered mineralization. Although several studies have examined the petrological, geochemical, geochronological, and tectonic characteristics of porphyry and related deposits in the region (e.g., Batkhishig et al., 2010; Wainwright et al., 2011; Batsaikhan et al., 2018; Davaasuren et al., 2021; Ganbat et al., 2023), and a few have utilized multispectral remote sensing for regional alteration mapping (e.g., Son et al., 2014; Son et al., 2019). Recent advances, such as the geological mapping based on RF of the Tsagaan-uul area by Badrakh et al. (2025), have demonstrated the potential of Machine learning (ML) techniques for

geological mapping; however, their application to mineral prospectivity assessment has not yet been explored in Mongolia. To address this gap, this study develops an integrated RF-based MPM framework to identify porphyry-type mineralization zones, validated using EnMAP hyperspectral data. The objectives are to: (1) integrate geological, geophysical, and remote sensing datasets to generate predictive prospectivity maps; (2) evaluate the relative importance of key predictor variables; and (3) validate RF-derived prospectivity results using EnMAP-based hydrothermal alteration mapping. The findings demonstrate that integrating machine learning with hyperspectral remote sensing provides a robust, data-driven approach to mineral exploration, offering a transferable framework applicable to other metallogenic provinces across Mongolia.

STUDY AREA AND GEOLOGICAL SETTINGS

Mongolia lies within the Central Asian Orogenic Belt, one of the largest and most complex accretionary orogenic systems on Earth (Şengör et al., 1993; Jahn et al., 2000; Windley et al., 2007; Xiao et al., 2018) (Fig. 1A). The country is divided into two major tectonic domains: the northern Caledonian orogen and the southern Hercynian (Variscan) orogen. These domains are separated by the Main Mongolian Lineament, a prominent regional structural boundary that differentiates predominantly Precambrian and Lower Paleozoic rocks in the north from mainly Lower to Upper Paleozoic rocks in the south (Amantov et al., 1970; Badarch et al., 2002) (Fig. 1B). The Gurvansaikhan island arc terrane, situated in the central part of Mongolia's southern domain, represents an important metallogenic province hosting several porphyry copper deposits, including Oyu Tolgoi, the largest in the country (Badarch et al., 2002). Many of these deposits are related to Devonian to Carboniferous subduction-related magmatic activity in southeastern Mongolia, making the Gurvansaikhan and adjacent Mandalovoo island arc terranes key targets for mineral exploration (Lamb and Cox, 1998; Batkhishig et al., 2010). Because the study area spans four 1:200,000 geological map sheets, these were merged and

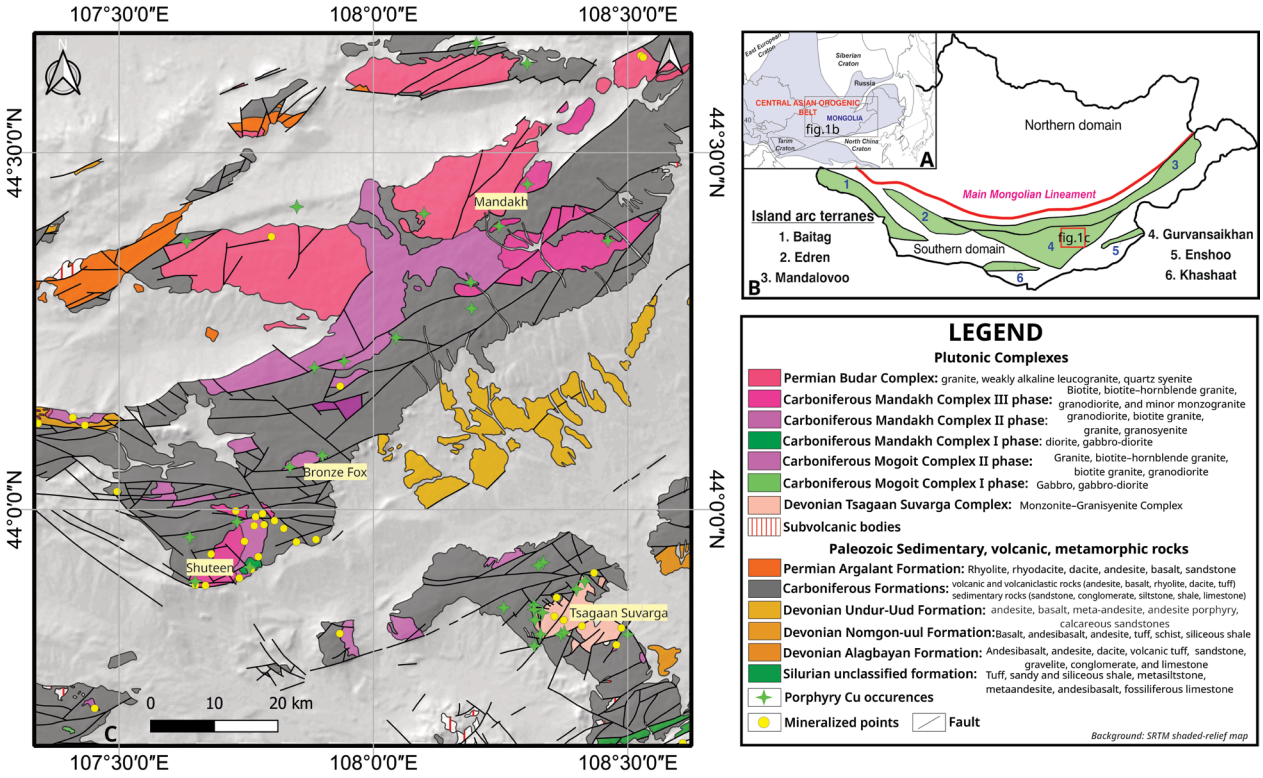

Fig. 1. Simplified geological map of the study area showing the distribution of plutonic complexes and Paleozoic sedimentary, volcanic, and metamorphic rocks. The map highlights major geological complexes, formations, and faults. Inset (A) shows a schematic map of the Central Asian Orogenic Belt (modified after Xiao et al., 2018); (B) the tectonic subdivision of Mongolia's major island arc terranes (1-6) (modified after Badarch et al., 2002)

harmonized to produce an integrated geological map for this research (Fig. 1C).

Magmatism in the region is represented by multiple intrusive phases ranging from the Devonian to Permian periods. The Devonian Tsagaan Suvarga Complex, composed of monzonite–granodiorite intrusions, represents the earliest phase of island-arc magmatism. In contrast, the Carboniferous Mandakh and Mogoit plutonic complexes comprise multiphase intrusive bodies including granitoid, granodiorite, quartz monzonite, and gabbro, and exhibit a strong spatial association with porphyry mineralization. The Permian Budar Complex represents a relatively late stage of magmatic activity and is dominated by weakly alkaline leucogranitic compositions. Additionally, subvolcanic bodies and dikes are widely developed across the area. Volcanic and sedimentary units of Devonian, Carboniferous, and Permian consist primarily of andesite, basalt, dacite, rhyolite, sandstone, limestone, and conglomerate lithologies (Delgertsogt et al., 2007; Nyamaa et al., 2013; Ariunchimeg et al., 2020) (Fig. 1C). Recent geochronological data indicated that the Undur-Uud Formation (Fig. 1) has a Carboniferous age of 338.6 ± 4.6 Ma (Munkhtsengel et al., 2018); however, this updated age attribution is not consistently reflected in existing regional geological maps, which are followed in this study

Porphyry Cu mineralization is predominantly concentrated along the margins of intrusive bodies and major fault zones, indicating that both structural and magmatic controls played a critical role in ore localization within the region.

A total of 33 porphyry-style mineralized deposits and occurrences were compiled and utilized as reference training data for mineral prospectivity mapping. These occurrences are of key significance in representing the metallogenic framework of the region and provide an essential basis for evaluating the spatial distribution and structural-magmatic controls of porphyry Cu mineralization. Among them, the Shuteen, Tsagaan Suvarga, Bronze Fox, and Mandakh areas are comparatively well-studied and considered advanced exploration targets. Their geological characteristics have been more extensively documented in previous studies. It is important to note that the lithostratigraphic unit names referenced in this study follow those used on the 1:200,000 geological maps.

The Tsagaan Suvarga deposit is a Late Devonian porphyry Cu-Mo system (364.9 ± 7 Ma; Lamb and Cox, 1998) situated along the northwestern margin of the Tsagaan Suvarga intrusive Complex. The mineralization is hosted by hornblende-biotite quartz monzonite and monzodiorite of subduction-related, I-type, high-K calc-alkaline affinity. Alteration is characterized by actinolite-biotite-chlorite-magnetite replacement of hornblende and primary biotite, overprinted by quartz-muscovite assemblages associated with Cu-Mo mineralization. Chalcopyrite and bornite are the primary ore minerals, with molybdenite occurring mainly within quartz-muscovite alteration zones (Tungalag et al., 2019). The delineated orebody measures approximately 2.0 × 0.5 km, with early resource estimates reporting 240 Mt at 0.53% Cu and 0.19% Mo (Japan International Cooperation Agency, 1992).

The Shuteen area comprises volcanic and intrusive rocks that were emplaced during multiple magmatic phases. The Shuteen Pluton intrudes Lower Carboniferous volcanic and sedimentary sequences. It consists of hornblende-biotite granite, granodiorite, quartz monzodiorite, monzonite, syenite, and diorite (Mandakh Complex in Fig. 1C). The intrusive suite records at least three magmatic stages accompanied by multiple generations of dykes, indicating a long-lived magmatic-hydrothermal system. Hydrothermal alteration is extensive, evolving from early potassic and propylitic assemblages to late-stage advanced argillic and silicic alteration, forming a prominent lithocap. Although no economic orebody has been identified to date, the alteration architecture suggests strong potential for a concealed porphyry Cu system at depth (Batkhishig et al., 2010; Batkhishig et al., 2014). U-Pb zircon and Rb-Sr isotopic ages indicate that the Shuteen intrusive phases formed at ~325 ± 1 Ma (Blight et al., 2010) and 321 ± 9 Ma (Iizumi and Batkhishig, 2000), respectively.

The Bronze Fox porphyry Cu-Au (Mo) deposit is mainly hosted by Early Carboniferous volcanic-sedimentary sequences, comprising marine sediments, tuffs, and conglomerates, overlain by the middle-late Carboniferous complex (Mandakh Complex in Fig. 1C) consisting of intermediate

to felsic volcanic rocks with interbedded sandstone and limestone. These sequences were subsequently intruded by multiple phases of granitoids, including granite, granodiorite, quartz monzodiorite, monzodiorite, diorite, quartz diorite, and tonalite porphyry (Ganbat et al., 2023). The granodiorite intrusion has a U-Pb zircon age of 333.6 ± 0.6 Ma (Blight et al., 2010). Mineral chemistry analyses of amphibole, biotite, and zircon suggest that the granodiorite intrusions at Bronze Fox are more favorable for the development of economic mineralization (Ganbat et al., 2023).

The Mandakh area, situated within the Gurvansaikhan and Manlai terranes, is underlain by Late Devonian-Carboniferous calc-alkaline, I-type to adakitic magmatic rocks, consisting predominantly of syenite, granite, and andesite-dacite volcanic units. These oxidized, subduction-related magmatic suites are considered fertile for porphyry Cu mineralization (Batsaikhan et al., 2018).

DATA AND METHODOLOGY

Data sources and predictor variables

A comprehensive set of geological, topographic, spectral, and geophysical datasets was compiled and integrated to develop the predictor variable database for the study area. All raster datasets were standardized to a 250 m spatial resolution and projected to the Universal Transverse Mercator Zone 48N coordinate system. The 250 m grid cell size was selected to align with the positional accuracy of the 1:200,000 geological map and to allow the integration of multi-resolution datasets (10 m, 30 m, and 0.05°) without introducing artificial spatial detail or scale-related bias. In data-driven mineral prospectivity mapping, the choice of raster resolution is a critical methodological decision, as each mineral occurrence should ideally be associated with a single raster unit cell to avoid spatial bias during model training (Carranza, 2009). This spatial resolution provides an optimal balance between maintaining key geological and geomorphological patterns across the ~100 km-wide study area and ensuring computational efficiency and model stability during training and prediction. Before modeling, all raster layers were co-registered to a common spatial extent, pixel origin, and grid alignment to eliminate spatial inconsistencies and to support accurate pixel-based analysis.

The predictor variables were selected based on established geological models of porphyry copper systems and the availability of regionally consistent datasets. The resulting set of 15 predictors captures the main structural, geophysical, topographic, and hydrothermal alteration controls on porphyry Cu mineralization, while remaining sufficiently limited to reduce overfitting in regional-scale, data-limited RF modeling. A total of 15 predictor variables were compiled into a multi-band raster stack at 250 m resolution (Table 1). These included Euclidean distance to faults, proximity to Devonian, Carboniferous, and Permian intrusive bodies, gravity anomaly, Shuttle Radar Topography Mission Digital Elevation Model (SRTM DEM), terrain derivatives, and seven Sentinel-2A-derived spectral alteration indices representing iron oxide, hydroxyl-bearing, and gossan-related mineralogical variations (van der Meer et al., 2014; van der Werff and van der Meer, 2016). Fault traces were digitized from the 1:200,000 geological map, rasterized, and converted into Euclidean distance rasters (m). Intrusive units were extracted from the same map and grouped into Devonian, Carboniferous, and Permian categories based on lithology and age. Each group was rasterized and transformed into Euclidean distance layers to serve as spatial proxies for magmatic-hydrothermal processes linked to porphyry Cu mineralization. Gravity data were obtained from the EIGEN-6C4 global gravity model (Förste et al., 2014) via the International Centre for Global Earth Models service (Ince et al., 2019) at a resolution of 0.05° (~4-5 km) and were subsequently resampled to 250 m.

Spectral alteration indices were generated from atmospherically corrected Sentinel-2A imagery, which provides 13 VNIR–SWIR bands at 10–60 m spatial resolution under the Copernicus program (EC/ESA). Four Level-2A scenes were used: S2A_MSIL2A_20250410T035201_N0511_R104_T48TXP_20250410T062701.SAFE, S2A_MSIL2A_20250410T035201_N0511_R104_T48TXQ_20250410T062701.SAFE, S2A_MSIL2A_20250427T034201_N0511_R061_T48TYP_20250427T061613.SAFE, S2B_MSIL2A_20250503T034539_

N0511_R104_T48TYQ_20250503T055513.SAFE.

The processed scenes were mosaicked, co-registered, and resampled to 10 m spatial resolution using bilinear interpolation. The final mosaic was clipped to the boundary of the study area to ensure consistent spatial coverage with other datasets. Indices were computed using NIR-SWIR band-ratio techniques following van der Meer et al. (2014) and van der Werff and van der Meer (2016). Topographic variables representing geomorphological conditions were derived from the SRTM DEM, including elevation, slope, and topographic position index (TPI). Slope reflects terrain gradients influencing erosion and exposure of lithologies, whereas TPI identifies relative topographic positions such as ridges and valleys that may correspond to structural or lithological controls (Weiss, 2001). SRTM DEM provides consistent radar-derived elevation data at 1-arc-second (~30 m) and 3-arc-second (~90 m) resolution (Farr et al., 2007). Although these morphometric variables are not commonly used as predictor inputs in ML-based MPM, a few recent studies have demonstrated their utility for capturing geomorphological controls on mineralization (Josso et al., 2023; Mahboob et al., 2024).

To evaluate the influence of geological knowledge on model performance, two RF model configurations were developed:

1. Model A (15 variables): included all predictors, including the three intrusion-proximity layers.
2. Model B (12 variables): excluded the intrusion-proximity layers, representing a geology-independent, data-driven configuration.

This dual-model design enables a direct comparison between a geologically informed model (Model A) and a neutral, data-driven model (Model B), thereby quantifying the added value of intrusion-related predictors for porphyry Cu prospectivity mapping.

Dataset generation

A total of 33 confirmed porphyry-style deposits and occurrences within the study area were used as the primary training dataset for model development. Because single coordinate points do not adequately represent the spatial footprint of porphyry systems, nor the extent of associated hydrothermal alteration halos, each occurrence was buffered by 1,000 m to capture spatial variability and account for positional uncertainty. To increase the number and spatial representativeness of training samples, three additional points were randomly generated within each buffer zone, resulting in 132 positive samples (class = 1). The approach is conceptually consistent with the spatial weighting strategy proposed by Harris et al. (2006), who emphasized increasing spatial representation around known deposits to strengthen training datasets when limited occurrences are available (Harris et al., 2025).

On the other hand, defining non-mineralized samples is inherently challenging in mineral prospectivity studies because areas without known deposits may still host undiscovered mineralization (Behnia et al., 2023). Following recommendations that non-deposit samples should be generated only beyond a minimum distance from known mineralization to minimize false negatives (Harris et al., 2025), a distance-based exclusion approach was adopted. To reduce the likelihood of misclassifying permissive ground as background, 34 additional mineralized points were used exclusively for exclusion purposes rather than as positive samples. Both the 33 porphyry occurrences and the 34 additional mineralized points were buffered by 3,000 m, dissolved, and removed from the sampling domain, resulting in a conservative background area that minimized false-negative selection. From this restricted zone, 132 random points were extracted as negative samples (class = 0), producing a balanced dataset of 264 labelled samples for training and testing. All spatial sampling procedures were conducted in QGIS v3.40.

RF classification workflow and prospectivity map generation

RF classifier (Breiman, 2001) was implemented using the *scikit-learn library* for mineral prospectivity modeling. The predictor set consisted of 15 continuous variables (Table 1), and a binary target (1 = mineralized, 0 = non-mineralized). Missing values were imputed

Table 1. Predictor variables used in the RF models

Types of predictors	Name of predictors	Original resolution/ data source	Resampled to (m)
Structural and geophysical variables	Distance to faults (m)	1:200,000 geological map	250
	Gravity anomaly (mGal)	EIGEN-6C4 (0.05° grid)	250
Geological context (Intrusion-related) *(used only in Model A)*	Distance to Carboniferous intrusions (m)	1:200,000 geological map	250
	Distance to Devonian intrusions (m)	1:200,000 geological map	250
	Distance to Permian intrusions (m)	1:200,000 geological map	250
Topographic variables (derived from SRTM-DEM)	Elevation (m)	30 m	250
	Slope (°)	30 m	250
	TPI	30 m	250
Spectral alteration indices (derived from Sentinel-2A reflectance)	Ferric iron (B4/B3)	10 m	250
	Ferrous iron (B12/B8 + B3/B4)	10-20 m*	250
	Gossan (B11/B4)	10-20 m*	250
	Ferrous silicates (B12/B11)	20 m	250
	Ferric oxides (B11/B8)	10-20 m*	250
	Iron oxides (B4/B2)	10 m	250
	OH-bearing alteration (B11/B12)	20 m	250

*Mixed-resolution indices use 10 m (B2, B3, B4, B8) and 20 m (B11, B12) bands. Compute at 20 m after aligning/ resampling the 10 m bands to 20 m, then resample the resulting index to 250 m.

using median substitution. The RF model was configured with 500 trees, the Gini impurity criterion, and max_features = "sqrt", a standard setting to enhance ensemble diversity in classification tasks (Breiman, 2001). Class imbalance was addressed using a balanced-subsample weighting scheme, and bootstrap aggregation was enabled with default tree-depth settings to preserve full data-driven complexity. To address spatial autocorrelation, an important concern in spatial data analysis, a group-aware train–test split was performed using 10 km spatial blocks, allocating 30% of the samples to independent testing. Model performance was assessed using out-of-bag error and a group-aware Receiver operating characteristic (ROC) analysis with bootstrap-derived 95% confidence intervals (CI) (Hanley and McNeil, 1982). The optimal decision threshold was selected using Youden's J statistic (Youden, 1950), and posterior probabilities were used to delineate the top 10% highest-ranked prospective zones. In addition, RF enables evaluation of predictor contributions through variable importance metrics, such as the Mean Decrease in Gini index, which ranks variables by their reduction in node impurity (Degenhardt et al., 2019). Raster predictions and final maps were generated in Python using the *rasterio* and *geopandas* libraries.

Integration with EnMAP hyperspectral validation

We independently cross-validated the RF prospectivity results using EnMAP hyperspectral imagery, which provides detailed spectral data for detecting hydrothermal alteration minerals linked to porphyry-style mineralization. Three EnMAP Level-2A surface reflectance scenes (30 m spatial resolution; UTM Zone 48N) that partly cover the central study area were pre-processed and combined into one hyperspectral data cube with the EnMAP-Box 3.16.3 plugin in QGIS. These scenes were collected on 5 October 2025 and include the following datasets: ENMAP01___L2ADT0000156113_20251005T042340Z_001_V010502_20251006T002020, ENMAP01___L2A-DT0000156113_20251005T042344Z_002_V010502_20251006T002018Z, ENMAP01___L2A-DT0000156113_20251005T042348Z_003_V010502_20251006T002020Z. Before mosaicking, we removed bands with low signal-to-noise ratios, atmospheric absorption, or missing data, which left a 167-band optimized subset for spectral analysis. We then applied reflectance scaling using the per-band gain factor (0.0001) and offset (0) from the ENVI header to convert digital numbers to surface reflectance (0-1). Because EnMAP only covers part of the

study area, we used the processed data cube only for extracting spectral indices and independently validating the RF-based prospectivity results, not for mapping the entire region.

Spectral Alteration Index Extraction and Validation

Porphyry copper deposits are typically surrounded by zoned hydrothermal alteration halos comprising potassic, phyllic, argillic, and propylitic assemblages, as described in the introduction. Short-wave infrared (SWIR) reflectance spectroscopy provides a rapid and effective means of detecting and characterizing hydrothermal alteration associated with ore-forming systems (Hauff, 2008; Neal et al., 2018). Before spectral analysis, the EnMAP SWIR data cube was subset to the 2150-2440 nm range to capture key absorption features of alteration minerals related to porphyry copper systems.

Continuum Removal (CR) was applied to this subset using the EnMAP-Box CR module to enhance subtle absorption features and allow consistent spectral comparison. To derive representative field-scale spectral profiles, a kernel-based sampling approach was adopted instead of single-pixel extraction to minimize noise, pixel-level variability, and sub-pixel mixing. Five occurrence points were selected from known deposits, including three within the Shuteen and two within the Bronze Fox. Spectra were extracted from 3 × 3 pixel kernels, averaged, and stored in an EnMAP-Box spectral library for subsequent comparison. CR was then applied to the kernel-averaged spectra to normalize and enhance diagnostic absorption features, enabling direct comparison of alteration mineral signatures across sites (Clark et al., 2003). The CR method fits a continuum across a defined wavelength interval and scales reflectance values relative to this baseline, thereby improving the visibility of absorption features associated with Al-OH and Mg-Fe-OH minerals which are key indicators of phyllic/argillic and propylitic alteration, respectively.

To validate and interpret the MPM results, alteration indices were derived from the EnMAP hyperspectral cube using band-depth analysis. Two diagnostic wavelength intervals were targeted: Al-OH (≈ 2130-2250 nm), indicative of phyllic-argillic alteration (sericite, muscovite, kaolinite), and Mg-Fe-OH (≈ 2250-2380 nm), indicative of propylitic alteration (chlorite, epidote).

Band-depth (BD) values were calculated following the standard formulation (Clark and Roush, 1984; Kokaly and Clark, 1999):

$$BD(\lambda) = 1 - \frac{R_b}{R_c} = 1 - R_{CR}(\lambda)$$

where R_b is the reflectance at the absorption minimum, R_c the continuum at that wavelength, and R_{CR} the continuum-removed reflectance. CR normalizes spectra by dividing the reflectance by the fitted continuum, thereby isolating and scaling absorption features between 0 and 1. Higher BD values indicate stronger absorption and, consequently, a greater relative abundance of the corresponding alteration minerals. To enable spatial comparison with the RF-based MPMs, the Al-OH and Mg-Fe-OH band-depth rasters derived from EnMAP were resampled to 250 m spatial resolution by mean aggregation, matching the RF model grid. Moreover, a Top 10% prospectivity mask was generated for each model by applying the 90th percentile (P90) threshold to the continuous RF probability outputs, where pixels ≥ P90 were assigned a value of 1. These binary Top 10% masks for Models A and B were then overlaid with the resampled alteration layers to quantify the spatial correspondence between highly prospective areas and hydrothermal alteration zones. The degree of overlap was computed for Al-OH, Mg-Fe-OH, and combined alteration layers, providing an independent validation of the MPM predictions.

RESULTS

Test Performance

A total of 264 labelled samples were prepared for model development, comprising 132 positive samples and 132 negative samples extracted from low-prospectivity background areas. This yielded a 70/30 train-test split, resulting in 166 training samples (83 positive and 83 negative) and 98 spatially independent test samples (Fig. 2).

RF models show contrasting predictive performances depending on whether intrusion-related predictors were included (Table 2).

Model A, which includes intrusion-distance

Table 2. Performance comparison between Model A (with intrusion predictors) and Model B (without intrusion predictors)

Metric	Model A	Model B
Number of predictors variables	15	12
Accuracy	0.837	0.714
Precision	0.844	0.714
Recall	0.837	0.714
F1-score	0.837	0.714
AUC	0.92	0.745

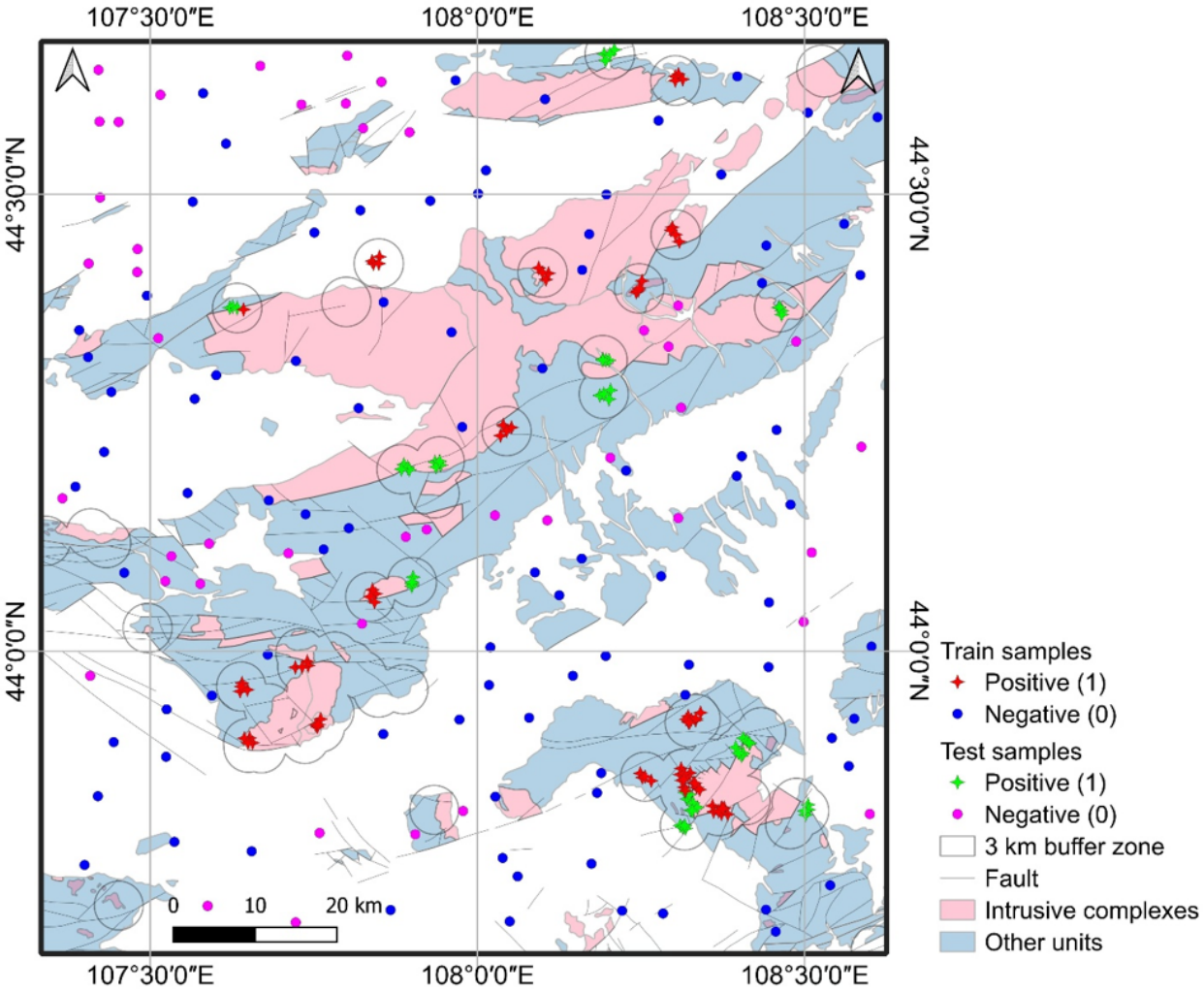

Fig. 2. Distribution of positive and negative training and testing samples overlaid on major geological units in the study area

variables, achieved an Area Under the Receiver Operating Characteristic Curve (AUC) of 0.920 with a 95% CI of 0.859-0.972 on the independent test set, indicating excellent discriminatory performance. The optimal probability threshold derived from Youden's J statistic was 0.302 (Fig. 3A). In contrast, Model B yielded a lower ROC-AUC of 0.745 (95% CI: 0.635-0.848) with an optimal threshold of 0.402 (Fig. 3B). Model A also achieved higher overall accuracy (0.837) than Model B (0.714).

Variable importance analysis reveals a clear shift in dominant predictors between the two models (Fig. 4). In Model A, the most important variables are distances to Carboniferous intrusions (0.152), Devonian intrusions (0.148), and distance to faults (0.125) (Fig. 5), followed by elevation (0.100). Distance to Permian intrusions (0.080)

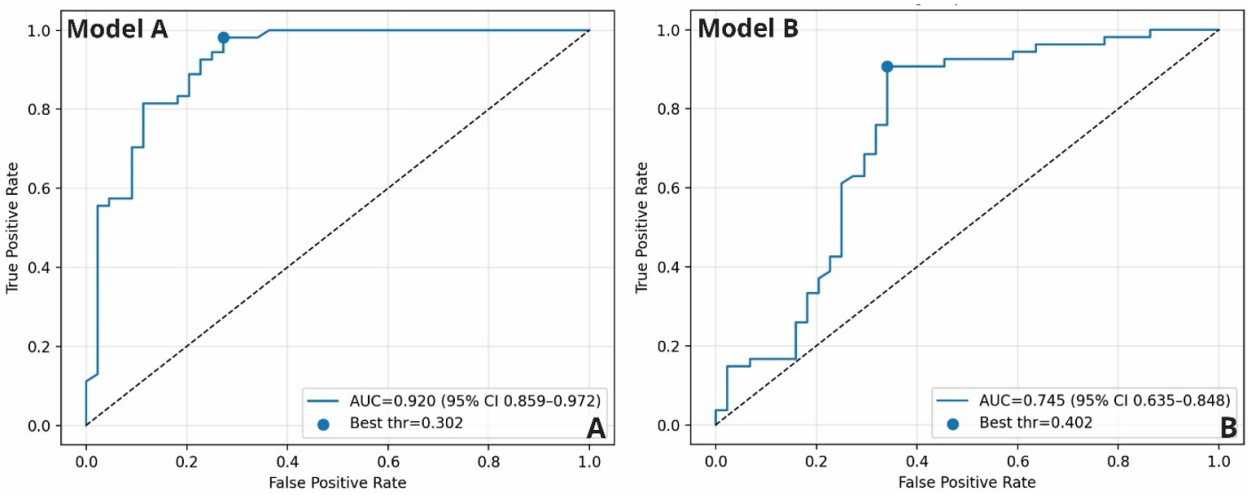

Fig. 3. ROC curves for the two RF prospectivity models. (A) Model A including intrusion-related predictors (n = 15); (B) Model B excluding intrusion-related predictors (n = 12)

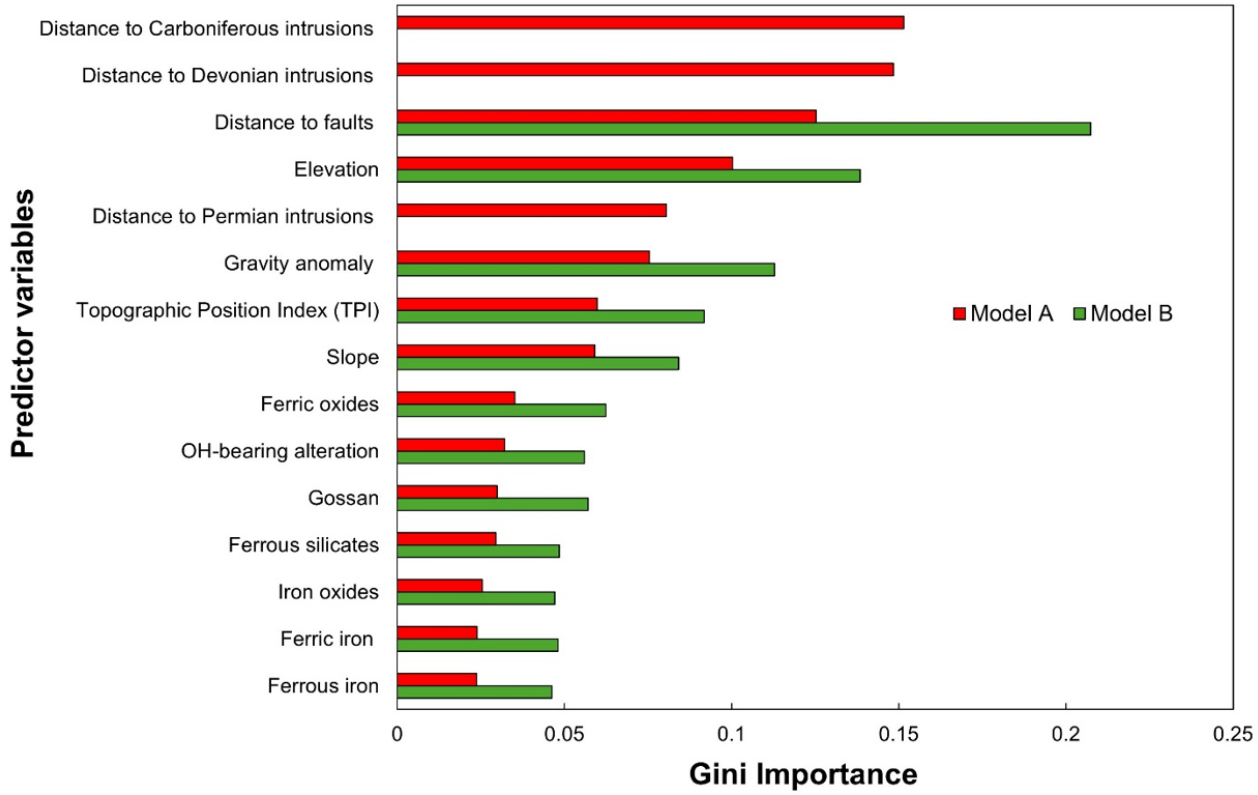

Fig. 4. Gini importance of predictor variables for Model A and Model B, showing the shift in dominant controls on prospectivity between the two models

and gravity anomaly (0.075) also contribute to model importance.

In Model B, distance to faults (0.207), elevation (0.138), and gravity anomaly (0.113) dominate predictor importance. Terrain-related variables such as TPI (0.092) and slope (0.084) also show increased influence. Spectral alteration indices contribute less individually (0.024-0.062) but remain informative in both models (Fig. 4).

Mineral prospectivity probability map

The RF-derived prospectivity maps illustrate the spatial distribution of predicted porphyry Cu potential, with values ranging from low (blue) to high (red) (Fig. 6). Model A delineates more continuous and spatially focused high-prospectivity zones, particularly in the central and southeastern parts of the study area, and shows a meaningful spatial correspondence with known porphyry deposits and prospects (Fig. 6A). Model

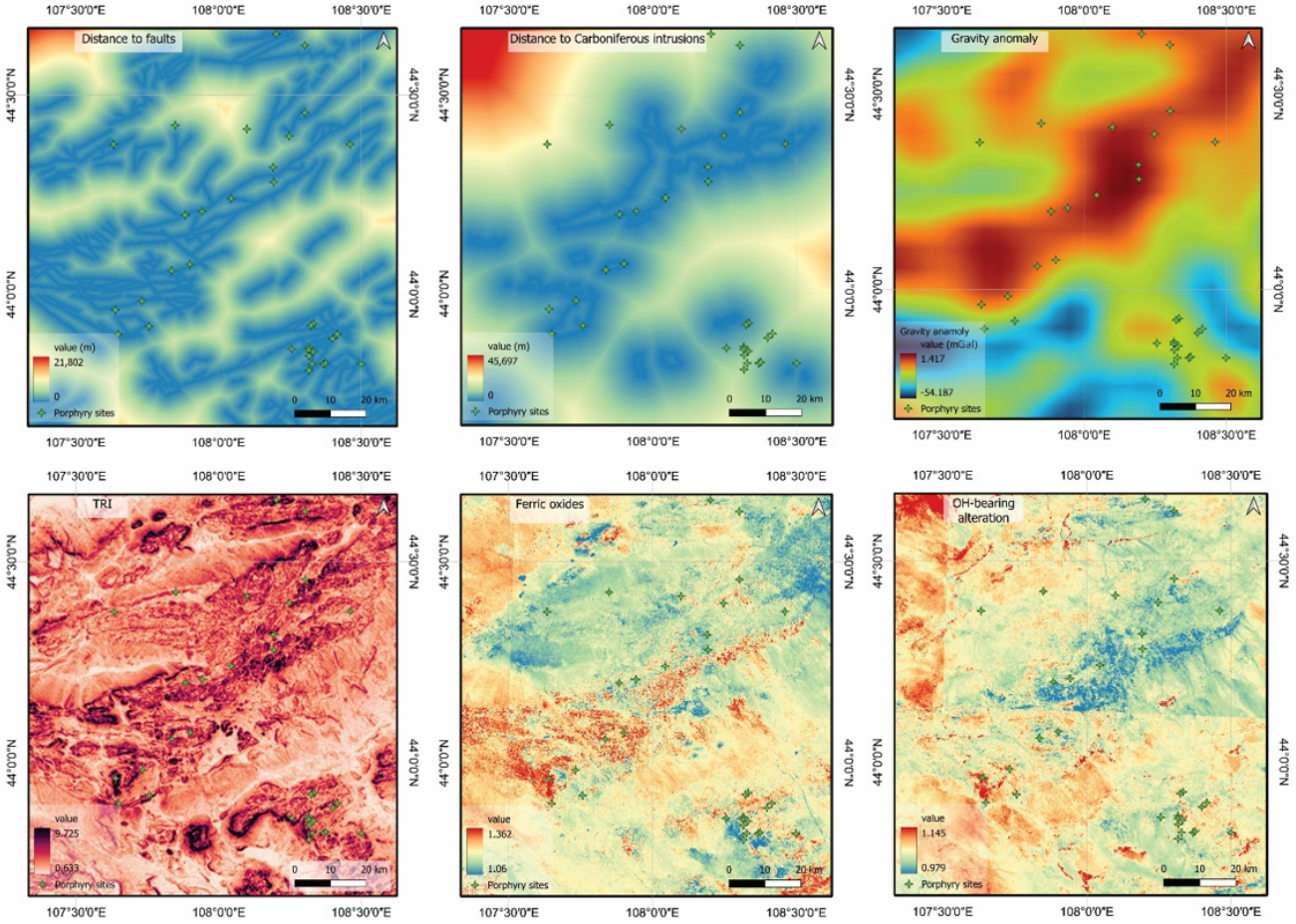

Fig. 5. Some of the most influential predictors for both models

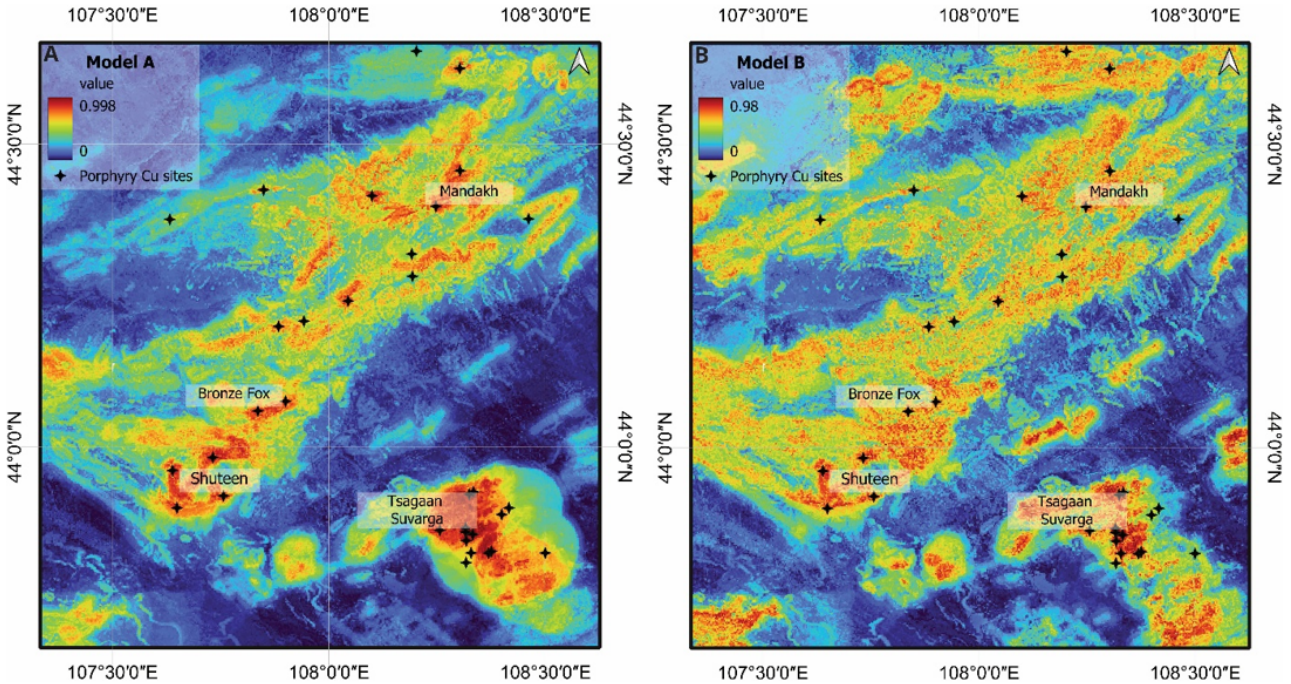

Fig. 6. RF-derived mineral prospectivity maps of the study area. (A) Model A; (B) Model B; The color scale represents the probability of porphyry Cu mineralization, ranging from low (0) to high (1). Black stars denote known porphyry Cu occurrences, plus well-studied areas including Shuteen, Bronze Fox, Mandakh, and Tsagaan Suvarga

B identifies similar clusters but exhibits more diffuse patterns with lower anomaly contrast (Fig. 6B).

Both models highlight additional areas of elevated prospectivity outside currently known occurrences, suggesting potential targets for future exploration.

EnMAP Alteration Mapping and Validation of the RF Model

EnMAP hyperspectral data were used to independently validate the RF-based prospectivity models by mapping hydrothermal alteration associated with porphyry Cu systems. A true-color composite (RGB: Bands 047, 032, and 013; Fig. 7) was first generated to highlight lithological contrasts, structural features, and known Cu occurrences. Because EnMAP coverage does not span the entire study area, alteration mapping and validation were restricted to the area covered by the EnMAP scene.

Comparison of EnMAP-Derived and Sentinel-2 Spectral Indices.

We created a set of alteration-specific spectral indices from the EnMAP data (Shebl et al., 2025) (Table 3) and compared them with analogous Sentinel-2A indices (van Der Meer et al., 2014; van der Werff and van der Meer, 2016) (Table 1) to evaluate the added value of hyperspectral information for detecting hydrothermal alteration. The comparison focused on OH-

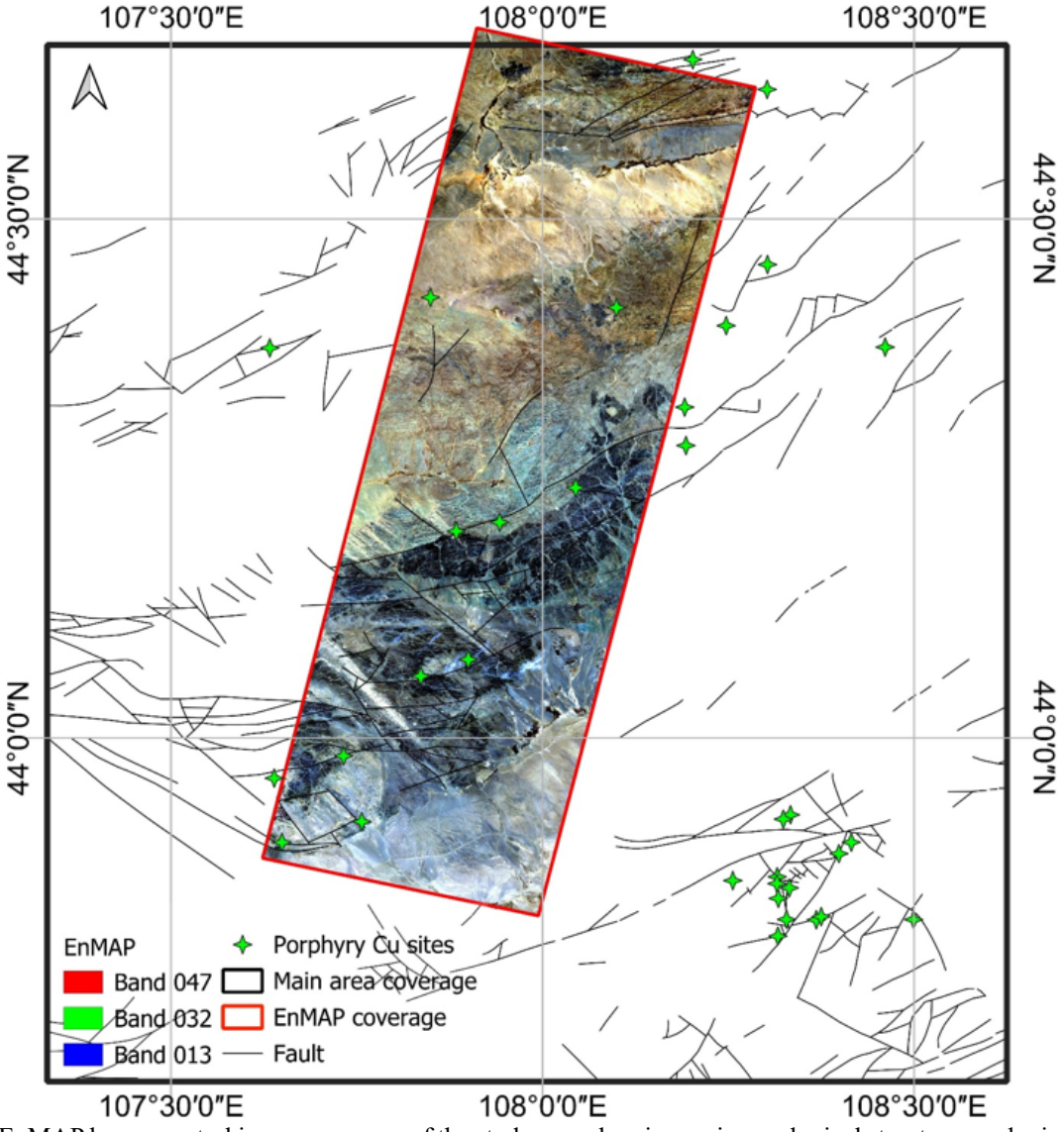

Fig. 7. EnMAP hyperspectral image coverage of the study area showing major geological structures and mineral occurrences

Table 3. EnMAP spectral indices, band ratios, and corresponding wavelengths used for alteration mapping (Shebl et al., 2025)

Indices	Band ratio	Corresponding wavelengths (nm)
OH-bearing alteration	B150 / B224	1609.02, 2445.3
Mg-Fe-OH minerals	(B201 + B218)/B209	2265.79, 2400.00, 2330.05
Iron-bearing minerals	B48/B16	666.63, 491.78
Al-OH minerals	(B189 + B201)/B194	2165.47, 2265.79, 2207.86

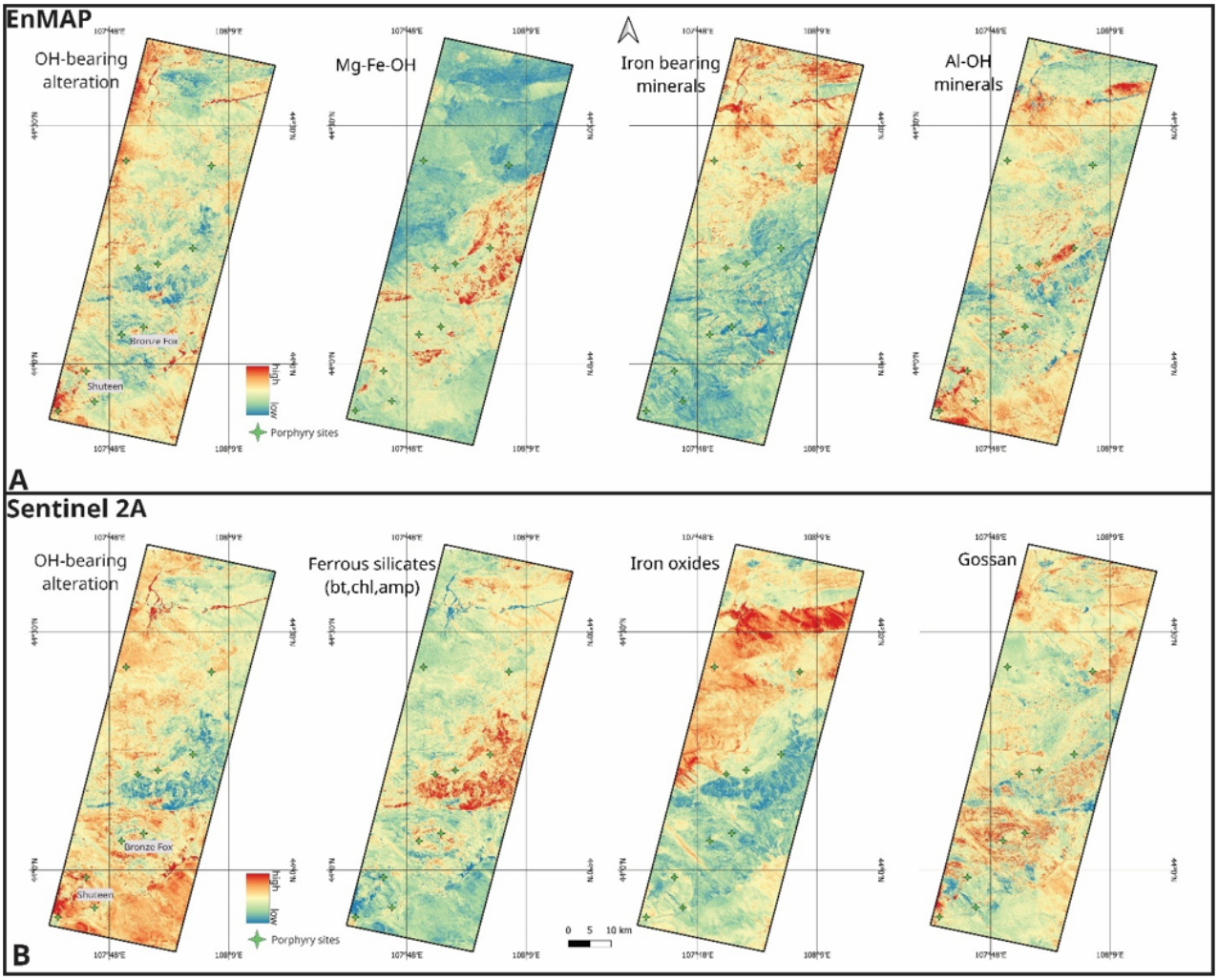

Fig. 8. EnMAP and Sentinel-2A derived alteration index maps for the study area. (A) EnMAP maps illustrating OH-bearing alteration, Mg-Fe-OH minerals, iron-bearing minerals, and Al-OH minerals; (B) Sentinel-2A maps showing OH-bearing alteration, ferrous silicates (biotite-chlorite-amphibole), iron oxides, and gossan

bearing alteration, Al-OH minerals, Mg-Fe-OH assemblages, iron-bearing minerals, and gossan indicators (Fig. 8).

The results show that both sensors generally capture the main alteration patterns. However, EnMAP-derived indices reveal clearer and more spatially continuous mineralogical zones. Although both datasets were analyzed at a common spatial resolution of 30 m after resampling, EnMAP's higher spectral resolution, particularly in the SWIR region, allows more accurate detection of diagnostic absorption features. As a result, phyllic (Al-OH) and propylitic (Mg-Fe-OH) alteration zones are more sharply defined in EnMAP (Fig. 8A). Sentinel-2A indices show similar patterns but with reduced clarity due to fewer SWIR bands (Fig. 8B).

Spectral characterization and alteration mapping

Continuum-removed spectra from the Shuteen and Bronze Fox porphyry systems reveal

diagnostic absorption features in two main SWIR intervals: 2130-2250 nm for Al-OH and 2230-2380 nm for Mg-Fe-OH. These intervals were used for BD mapping to delineate argillic/phyllic and propylitic alteration zones (Fig. 9A).

The resulting alteration masks show clear hydrothermal zonation, with Al-OH alteration concentrated near the Shuteen and Bronze Fox centers and Mg-Fe-OH alteration forming wider haloes around the Al-OH cores. Continuum-removed spectra from five sample locations (three in Shuteen and two in Bronze Fox) confirm these patterns (Fig. 9B-C). Absorptions near 2200 nm indicate white mica (muscovite-illite) associated with phyllic alteration, while features at 2248-2266 nm and 2337-2368 nm correspond to Mg-Fe-OH vibrations in chlorite-epidote assemblages, indicating propylitic alteration. BD-derived products provide more continuous alteration boundaries than index-based maps.

Validation of the RF prospectivity model. To ensure spatial consistency between the EnMAP-derived alteration maps and the RF-based MPMs (Fig. 10A, C), the Al-OH and Mg-Fe-OH alteration maps were resampled to 250 m resolution. High-prospectivity zones were defined as the top 10% of prospectivity values (≥90th percentile) from each RF model. These areas were overlaid with the alteration masks to quantify spatial correspondence (Fig. 10B, D).

For Model A, 22.23% of high-prospectivity pixels overlap with Al-OH alteration, 9.91% with Mg-Fe-OH alteration, and 31.12% with either alteration type. For Model B, the corresponding

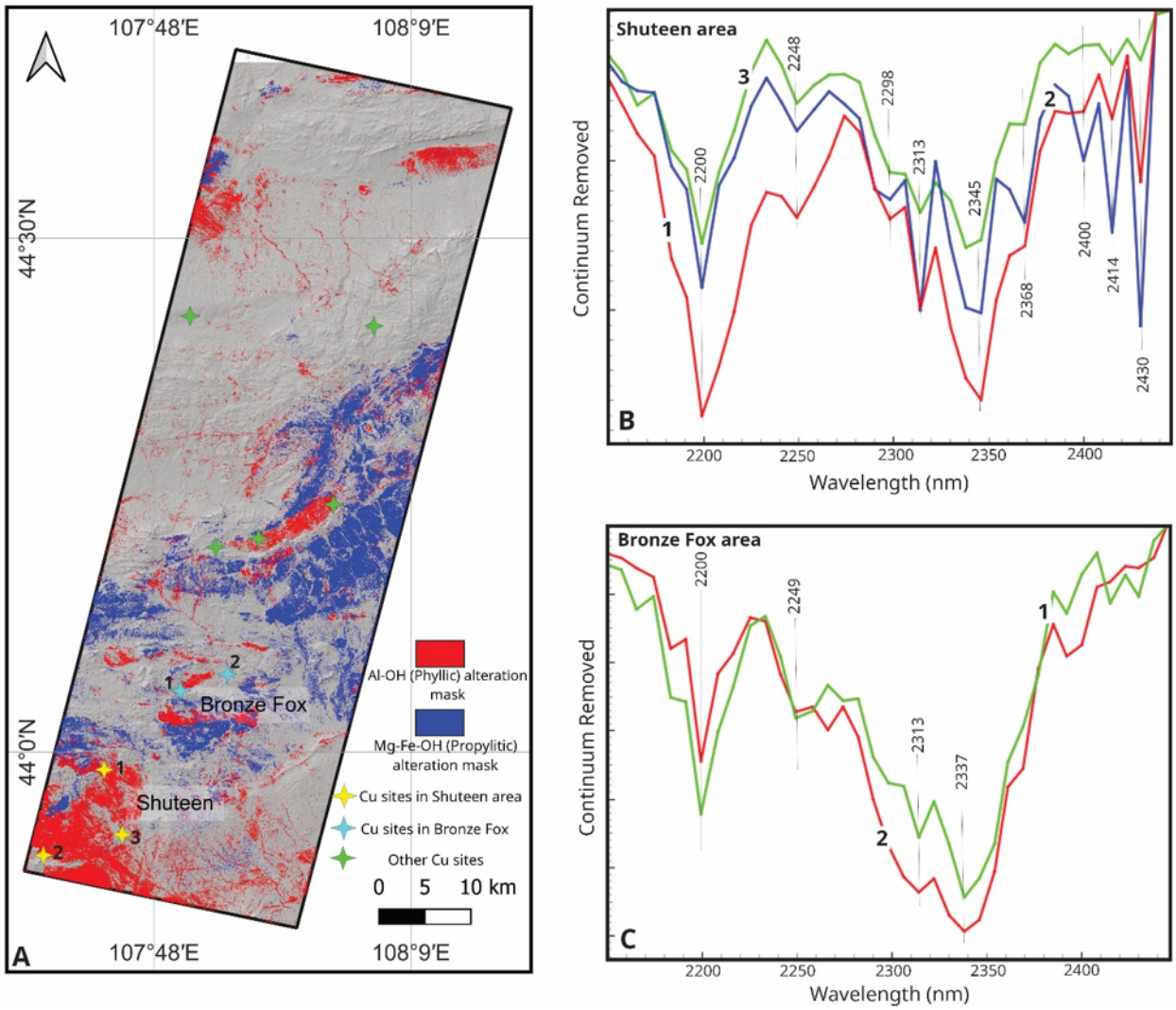

Fig. 9. (A) Hydrothermal alteration masks derived from EnMAP SWIR CR analysis, illustrating the spatial distribution of Al-OH (argillic/phyllic) and Mg-Fe-OH (propylitic); (B) CR EnMAP spectra for three representative samples from the Shuteen area; (C) CR spectra for two representative samples from the Bronze Fox area

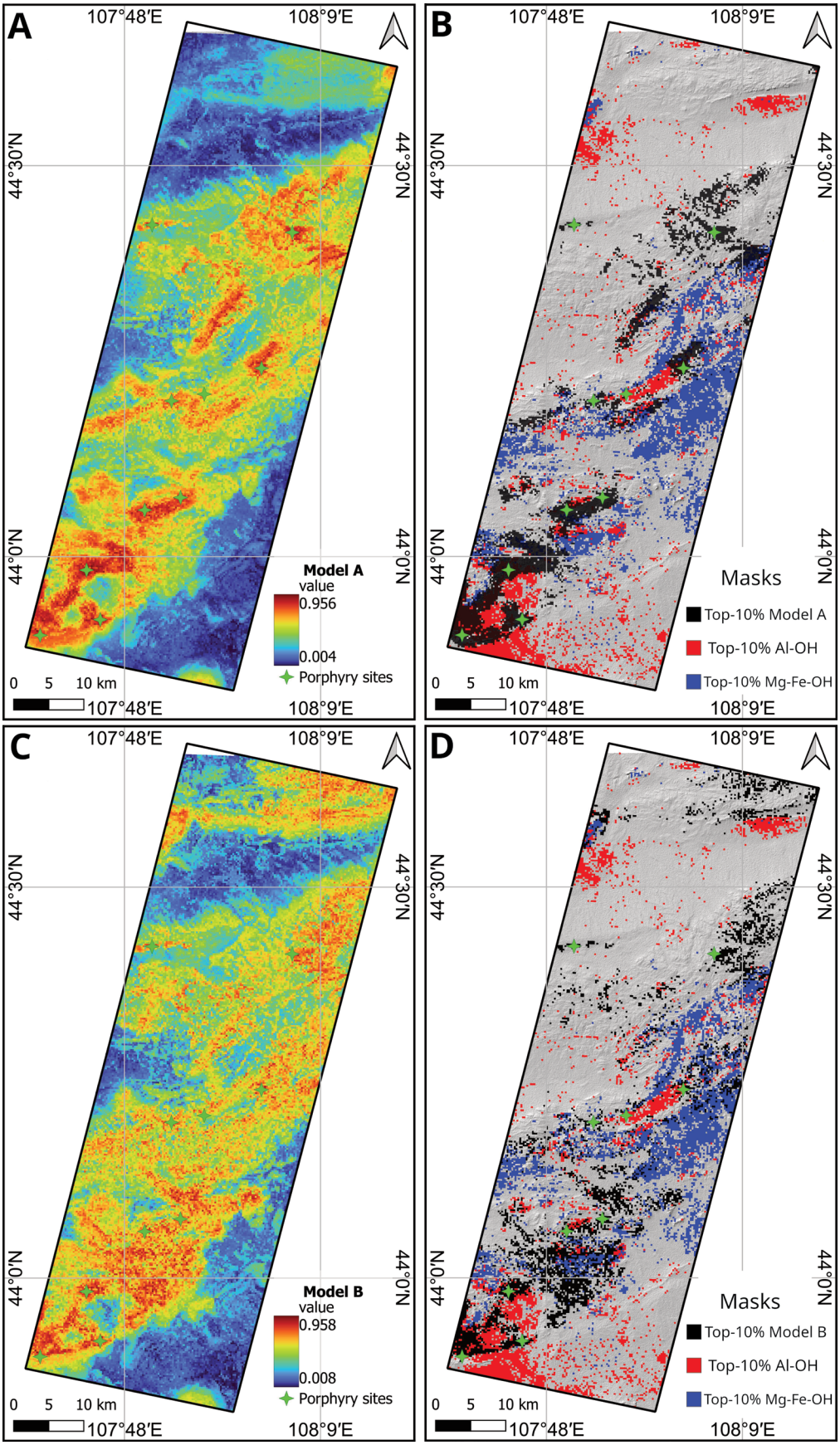

Fig. 10. Spatial overlap between RF prospectivity maps and EnMAP-derived alteration zones. (A) RF prospectivity map for Model A (including intrusion-related predictors); (B) Spatial overlap between the top-10% high-prospectivity pixels of Model A and EnMAP-derived Al-OH and Mg-Fe-OH alteration masks; (C) RF prospectivity map for Model B (excluding intrusion-related predictors); (D) Spatial overlap between the top-10% high-prospectivity pixels of Model B and the Al-OH and Mg-Fe-OH alteration masks

Table 4. Overlap statistics between Top 10% prospectivity pixels and alteration masks

Metric	Top 10% of MPM	Overlap with Al-OH	Overlap with Mg-Fe-OH	Combined Alterations
Pixel count	4399	978	436	1369
% of Top 10 Model A	100%	**22.23%**	**9.91%**	**31.12%**

Metric	Top 10% of MPM	Overlap with Al-OH	Overlap with Mg-Fe-OH	Combined Alterations
Pixel count	4368	728	533	1225
% of Top 10 Model B	100%	**16.67%**	**12.20%**	**28.04%**

overlaps are 16.67%, 12.20%, and 28.04%, respectively (Table 4). Model A shows stronger spatial alignment with Al-OH alteration, consistent with proximal alteration halos in porphyry systems.

DISCUSSION

Influence of predictor variable selection and dominance of intrusion proximity

Choosing the right predictor variables is key to how well MPMs perform and how broadly they can be applied (Sun et al., 2020). Geophysical datasets, particularly aeromagnetic and radiometric products, are commonly used in mineral prospectivity mapping and are important indicators of mineralization when combined with geological information (Sun et al., 2024). In this study, however, consistent regional geophysical coverage was unavailable, which limited the inclusion of such datasets. As a result, the modeling framework relied on geological, structural, topographic, and Sentinel-2A-derived spectral indices, along with long-wavelength gravity from a global gravity field model. Without detailed geophysical inputs like magnetic and radiometric data, the model was likely less able to detect deeper or more subtle features that are often important in porphyry Cu exploration (e.g., Clark, 2014; Anderson et al., 2023).

Despite these limitations, the selected predictors effectively captured the principal processes governing porphyry Cu systems. Intrusion-proximity variables served as spatial proxies for magmatic heat and metal sources (Porwal and Kreuzer, 2010), while structural and topographic parameters reflected hydrothermal fluid pathways and geomorphic responses. This process-based design ensured geological relevance despite data constraints.

Model performance improved substantially when intrusion-related predictors were included (AUC = 0.920), supporting the fundamental genetic link between porphyry systems and granitoid intrusions (Sillitoe, 2010). Distance to Devonian and Carboniferous intrusions were the most influential variables, consistent with known associations such as Shuteen and Bronze Fox with Carboniferous intrusions, and Tsagaan Suvarga with Devonian intrusions. This dominance reflects geological reality rather than model bias, as porphyry Cu mineralization in southern Mongolia is closely linked to subduction-related Devonian-Carboniferous magmatism (Batkhishig et al., 2010; Batsaikhan et al., 2018).

Some correlation among predictors is expected in geological systems. RF models are robust to correlated variables, although shared explanatory information may affect the relative ranking of variable importance (Breiman, 2001; Belgiu and Drăguţ, 2016). Consequently, variable importance results are interpreted in a comparative and process-based manner rather than as absolute measures of individual predictor significance.

The model performance may decrease in regions where the relationship between mineralization and intrusions is weaker or poorly mapped. Future studies could improve generalization by testing alternative intrusion datasets, subdividing intrusive phases using geochemical or geochronological criteria, and incorporating additional geophysical and structural metrics.

Integration of MPM and EnMAP-based validation

Independent validation of data-driven mineral prospectivity models remains challenging due to spatial autocorrelation, uneven sampling, and the lack of standardized validation frameworks (Koldasbayeva et al., 2024). In this study, EnMAP hyperspectral data were used as an independent

validation dataset to assess whether RF-predicted high-prospectivity zones spatially coincide with surface expressions of hydrothermal alteration. Although hyperspectral coverage was limited to a subset of the study area, its use exclusively for validation, rather than as a predictor, reduces circular reasoning and limits spatial dependence between modeling and validation data.

Two diagnostic SWIR alteration proxies, Al-OH and Mg-Fe-OH, were selected instead of detailed mineral identification. This approach was justified due to the limited mineralogical characterization of local porphyry systems and the robustness and transferability of Al-OH and Mg-Fe-OH indices across different lithologies (Clark, 2014).

The observed moderate to strong spatial correspondence between RF-derived high-prospectivity zones and Al-OH and Mg-Fe-OH anomalies using EnMAP suggests that the model predictions are broadly consistent with surface hydrothermal alteration patterns. This agreement between statistical predictions and mineralogical evidence supports the effectiveness of key predictors such as intrusion proximity, fault density, and topographic indices in representing the geological processes controlling porphyry Cu mineralization in southern Mongolia.

Strengths, limitations, and opportunities for future research

The observed spatial correspondence between RF-based prospectivity maps and EnMAP-derived alteration patterns enhances confidence in the modeling results and demonstrates the value of hyperspectral data for independent validation. Nevertheless, several limitations should be mentioned. First, EnMAP-based validation is restricted to the spatial extent of available imagery and may not capture full regional variability. Second, SWIR-based alteration mapping reflects surface expressions and may fail to detect concealed or deeply eroded mineral systems. Third, Al-OH and Mg-Fe-OH anomalies can also result from non-porphyry processes, underscoring the need for careful geological interpretation.

Future work should focus on (1) integrating regional airborne geophysics to improve detection of MPMs, and (2) validating alteration minerals using field spectrometer measurements or by comparison with reference spectra from the United States Geological Survey (USGS) spectral library to ensure mineralogical accuracy. Together, these advancements will make data-driven mineral prospectivity models easier to interpret, more adaptable, and more realistic from a geological perspective. Integrating RF-based MPMs with EnMAP-derived alteration analysis provides a scalable and geologically sound approach for porphyry copper exploration in Mongolia.

CONCLUSION

Porphyry copper deposits in the Gurvansaikhan terrane of southern Mongolia have been extensively studied in terms of geochemistry, petrography, and geochronology, yet the application of remote sensing, machine learning, and hyperspectral techniques has remained limited. This study addresses this gap by presenting an integrated framework that combines RF-based mineral prospectivity mapping with independent validation using EnMAP hyperspectral data.

The first stage of this study involved developing the RF machine learning models trained on 15 predictor variables derived from geological, structural, topographic, geophysical, and multispectral datasets. Since porphyry deposits are genetically associated with granitoid-porphyry intrusions, the inclusion of the intrusion proximity variables resulted in a high predictive performance, particularly influenced by the Devonian-Carboniferous intrusion-related occurrences. A second model excluding intrusion proximity variables demonstrated reduced performance, with prospectivity controlled primarily by structural, topographic, and gravity-related predictors, highlighting the influence of geological prior knowledge on model outcomes.

Independent validation using EnMAP hyperspectral data further strengthened the geological support for the RF results. CR analysis in diagnostic SWIR regions delineated argillic/phyllic (Al-OH) and propylitic (Mg-Fe-OH) alteration zones consistent with classical porphyry copper alteration models. Spatial overlap between high-prospectivity zones and alteration anomalies reveals that 31.12% of the top-decile RF targets in Model A and 28.04% in Model B coincide with alteration zones, indicating a moderate level of

spatial agreement. These findings indicate that hyperspectral CR alteration mapping provides independent, mineralogically grounded support for data-driven mineral prospectivity modeling.

From an exploration application perspective, MPM is a quantitative, data-driven approach that can enhance the efficiency of mineral exploration. It integrates various geoscientific datasets within a GIS environment, transforming spatial data into actionable information to support informed decision-making. In this study, the resulting maps provide a practical framework for regional exploration targeting and prioritization in southern Mongolia. By combining prospectivity modeling with hyperspectral alteration validation, this method objectively ranks high-probability targets and directs exploration to areas where subsurface features match surface alteration signatures. This is especially useful in Mongolia, where areas such as the Gurvansaikhan terrane are large, remote, and underexplored, and where exploration resources are limited. Consequently, the proposed framework can contribute to reducing exploration risk and improving the efficiency of resource allocation during early-stage regional exploration programs.

ACKNOWLEDGMENTS

The authors sincerely thank MSc. Erdenechimeg D. and the Geo-Information Center of the National Geological Survey of Mongolia for providing access to geological data and reports used in this research. The authors are also grateful to the editor and anonymous reviewers for their constructive comments and suggestions, which helped improve the quality of this manuscript.

Author contributions

Munkhsuren Badrakh: Writing - original draft preparation, Visualization, Validation, Methodology, Conceptualization. **Gáspár Albert:** Writing - reviewing and editing, Validation, Supervision, Conceptualization.

Competing interest

The authors declare that they have no known competing financial interests or personal relationships that could have appeared to influence the work reported in this paper.

REFERENCE

Abedi, M., Norouzi, G.-H., Bahroudi, A. 2012. Support vector machine for multi-classification of mineral prospectivity areas: Computers & Geosciences, v. 46, p. 272-283. https://doi.org/10.1016/j.cageo.2011.12.014

Ali Hosseini, S., Abedi, M. 2015. Data Envelopment Analysis: A knowledge-driven method for mineral prospectivity mapping: Computers & Geosciences, v. 82, p. 111-119. https://doi.org/10.1016/j.cageo.2015.06.006

Amantov, V.A., Blagonravov, V.A., Borzakovsky, Yu.A., Durante, M.V., Zonenshain, L.P., Luvsandanzan, Matrosov, P.S., Suetenko, O.D., Filippova, L.B., Khasin, R.A. 1970. Main features of stratigraphy of the Mongolian People's Republic: in Marinov, N.A., ed., Stratigraphy and Tectonics of the Mongolian People's Republic: Moscow, Nauka, p. 8-63 (in Russian).

Anderson, E.D., Yager, D.B., Deszcz-Pan, M., Hoogenboom, B.E., Rodriguez, B.D., Smith, B.D. 2023. Geophysical data provide three dimensional insights into porphyry copper systems in the Silverton caldera, Colorado, USA: Ore Geology Reviews, v. 152, p. 105223. https://doi.org/10.1016/j.oregeorev.2022.105223

Ariunchimeg, Ya., Orolmaa, D., Dejidmaa, G., Narantsetseg, Ts., Oyunchimeg, T., Udaanjargal, Kh., Enkhtuya, J., Urjinkhand, B., Suvd-Erdene, S., Bilguun, B., Tumenjargal, B., Myagmarnaran, D., Batzorig, G. 2020. Summary report on the compilation of the national 1:200,000-scale integrated geological maps of Mongolia for K sheets: Report No. 9820, Geological Information Center, Ulaanbaatar (in Mongolian).

Asadzadeh, S., Chabrillat, S., Cudahy, T., Rashidi, B., De Souza Filho, C.R. 2024a. Alteration mineral mapping of the Shadan Porphyry Cu-Au deposit (Iran) using airborne imaging spectroscopic data: implications for exploration drilling: Economic Geology, v. 119, p. 139-160. https://doi.org/10.5382/econgeo.5041

Asadzadeh, S., Koellner, N., Chabrillat, S. 2024b. Detecting rare earth elements using EnMAP hyperspectral satellite data: a case study from Mountain Pass, California: Scientific Reports, v. 14, p. 20766.

https://doi.org/10.1038/s41598-024-71395-2

Asadzadeh, S., Zhou, X., Chabrillat, S. 2024c. Assessment of the spaceborne EnMAP hyperspectral data for alteration mineral mapping: a case study of the Reko Diq porphyry Cu-Au deposit, Pakistan: Remote Sensing of Environment, v. 314, p. 114389. https://doi.org/10.1016/j.rse.2024.114389

Asadzadeh, S., Chabrillat, S. 2025. Leveraging EnMAP hyperspectral data for mineral exploration: examples from different deposit types: Ore Geology Reviews, v. 186, p. 106912. https://doi.org/10.1016/j.oregeorev.2025.106912

Badarch, G., Dickson Cunningham, W., Windley, B.F. 2002. A new terrane subdivision for Mongolia: implications for the Phanerozoic crustal growth of Central Asia: Journal of Asian Earth Sciences, v. 21, p. 87-110. https://doi.org/10.1016/S1367-9120(02)00017-2

Badrakh, M., Tserendash, N., Choindonjamts, E., Albert, G. 2025. Potential of random forest machine learning algorithm for geological mapping using PALSAR and Sentinel-2A remote sensing data: a case study of Tsagaan-uul area, southern Mongolia: Journal of Asian Earth Sciences: X, v. 14, p. 100204. https://doi.org/10.1016/j.jaesx.2025.100204

Batkhishig, B., Noriyoshi, T., Greg, B. 2010. Magmatism of the Shuteen Complex and Carboniferous subduction of the Gurvansaikhan terrane, South Mongolia: Journal of Asian Earth Sciences, v. 37, p. 399-411. https://doi.org/10.1016/j.jseaes.2009.10.004

Batkhishig, B., Noriyoshi, T., Bignall, G. 2014. Magmatic-hydrothermal activity in the Shuteen area, South Mongolia: Economic Geology, v. 109, p. 1929-1942. https://doi.org/10.2113/econgeo.109.7.1929

Batsaikhan, U., Noriyoshi, T., Anaad, C., Bayaraa, B. 2018. Petrochemical characteristics of late Paleozoic magmatic rocks of the Mandakh area, southeast Mongolia: Mongolian Geoscientist, v. 47, p. 5-21. https://doi.org/10.5564/mgs.v0i47.1061

Behnia, P., Harris, J., Sherlock, R., Naghizadeh, M., Vayavur, R. 2023. Mineral prospectivity mapping for orogenic gold mineralization in the Rainy River area, Wabigoon Subprovince: Minerals, v. 13, p. 1267. https://doi.org/10.3390/min13101267

Blight, J.H.S., Crowley, Q.G., Petterson, M.G., Cunningham, D. 2010. Granites of the Southern Mongolia Carboniferous arc: new geochronological and geochemical constraints: Lithos, v. 116, p. 35-52. https://doi.org/10.1016/j.lithos.2010.01.001

Bonham-Carter, G.F. 1994. Geographic Information Systems for Geoscientists: Modelling with GIS: Oxford, Pergamon, 398 p.

Breiman, L. 2001. Random forests: Machine Learning, v. 45, p. 5-32. https://doi.org/10.1023/A:1010933404324

Belgiu, M., Drăguţ, L. 2016. Random forest in remote sensing: A review of applications and future directions. ISPRS Journal of Photogrammetry and Remote Sensing, v. 114, p.24-31. https://doi.org/10.1016/j.isprsjprs.2016.01.011

Carranza, E.J.M. 2009. Objective selection of suitable unit cell size in data-driven modeling of mineral prospectivity. Computers & Geosciences, v35(10), p.2032-2046. https://doi.org/10.1016/j.cageo.2009.02.008

Carranza, E.J.M., Laborte, A.G. 2015. Data-driven predictive mapping of gold prospectivity, Baguio district, Philippines: application of Random Forests algorithm: Ore Geology Reviews, v. 71, p. 777-787. https://doi.org/10.1016/j.oregeorev.2014.08.010

Chabrillat, S., Foerster, S., Segl, K., Beamish, A., Brell, M., Asadzadeh, S., Milewski, R., Ward, K.J., Brosinsky, A., Koch, K., Scheffler, D., Guillaso, S., Kokhanovsky, A., Roessner, S., Guanter, L., Kaufmann, H., Pinnel, N., Carmona, E., Storch, T., Hank, T., Berger, K., Wocher, M., Hostert, P., Van Der Linden, S., Okujeni, A., Janz, A., Jakimow, B., Bracher, A., Soppa, M.A., Alvarado, L.M.A., Buddenbaum, H., Heim, B., Heiden, U., Moreno, J., Ong, C., Bohn, N., Green, R.O., Bachmann, M., Kokaly, R., Schodlok, M., Painter, T.H., Gascon, F., Buongiorno, F., Mottus, M., Brando, V.E., Feilhauer, H., Betz, M., Baur, S., Feckl, R., Schickling, A., Krieger, V., Bock, M., La Porta, L., Fischer, S. 2024. The EnMAP spaceborne imaging spectroscopy mission: initial scientific results two years after launch: Remote Sensing of

Environment, v. 315, p. 114379. https://doi.org/10.1016/j.rse.2024.114379

Clark, R.N., Roush, T.L. 1984. Reflectance spectroscopy-quantitative analysis techniques for remote sensing applications: Journal of Geophysical Research, v. 89, p. 6329-6340

Clark, R.N., Swayze, G.A., Livo, K.E., Kokaly, R.F., Sutley, S.J., Dalton, J.B., McDougal, R.R., Gent, C.A. 2003. Imaging spectroscopy: Earth and planetary remote sensing with the USGS Tetracorder and expert systems: Journal of Geophysical Research: Planets, v. 108, p. 2002JE001847. https://doi.org/10.1029/2002JE001847

Clark, D.A. 2014. Magnetic effects of hydrothermal alteration in porphyry copper and iron-oxide copper-gold systems: a review: Tectonophysics, v. 624-625, p. 46-65. https://doi.org/10.1016/j.tecto.2013.12.011

Cooke, D.R., Hollings, P., Walshe, J.L. 2005. Giant porphyry deposits: characteristics, distribution, and tectonic controls: Economic Geology, v. 100, p. 801-818. https://doi.org/10.2113/gsecongeo.100.5.801

Daoud, A.M.A., Shebl, A., Nafi, M., Elrasheed, A.A., Csámer, Á., Rózsa, P. 2025. Machine learning-based lithological mapping and mineral prospecting using hyperspectral and multispectral remote sensing in Wadi Halfa, north Sudan: Journal of African Earth Sciences, v. 232, p. 105816. https://doi.org/10.1016/j.jafrearsci.2025.105816

Davaasuren, O.-E., Koh, S.-M., Kim, N., Lee, B.H. 2021. Late Paleozoic adakitic magmatism in the Zogdor Cu occurrences, southern Mongolia, and their tectonic implications: new SHRIMP zircon age dating, Lu-Hf isotope systematics and geochemical constraints: Ore Geology Reviews, v. 138, p. 104356. https://doi.org/10.1016/j.oregeorev.2021.104356

Degenhardt, F., Seifert, S., Szymczak, S. 2019. Evaluation of variable selection methods for random forests and omics data sets: Briefings in Bioinformatics, v. 20, p. 492-503. https://doi.org/10.1093/bib/bbx124

Delgertsogt, B., Davga-Ochir, Ya., Munkhbat, Yo., Enkhtuya, Ch., Enkhjargal, S. 2007. Geological, mineral resource, Quaternary, and ecological-geological mapping at a scale of 1:200,000 in parts of Dornogovi and Dundgovi aimags (sheets L-49-XIX, XX, XXI, XXV, XXVI, XXVII, XXVIII, XXXI) under the "UGZ-200 Dornod Mongolia" project, 2005-2007: Report No. 5860, Geological Information Center, Ulaanbaatar (in Mongolian).

Farr, T.G., Rosen, P.A., Caro, E., Crippen, R., Duren, R., Hensley, S., Kobrick, M., Paller, M., Rodriguez, E., Roth, L., Seal, D., Shaffer, S., Shimada, J., Umland, J., Werner, M., Oskin, M., Burbank, D., Alsdorf, D. 2007. The Shuttle Radar Topography Mission: Reviews of Geophysics, v. 45, p. 2005RG000183. https://doi.org/10.1029/2005RG000183

Förste, C., Bruinsma, S.L., Abrikosov, O., Lemoine, J.-M., Marty, J.C., Flechtner, F., Balmino, G., Barthelmes, F., Biancale, R. 2014. EIGEN-6C4 The latest combined global gravity field model including GOCE data up to degree and order 2190 of GFZ Potsdam and GRGS Toulouse: International Centre for Global Earth Models (ICGEM). https://doi.org/10.5880/ICGEM.2015.1

Ganbat, B., Yang, X., Wang, Y., Odgerel, D., Faisal, M., Sanchir, D., Tsolmon, A., Munkhtur, E., Sun, C. 2023. Petrogenesis and geochronology of the Bronze Fox porphyry Cu-Au deposit: implications for the geodynamic evolution of the Gurvansaykhan Island arc, southern Mongolia: International Geology Review, v. 65, p. 2774-2797. https://doi.org/10.1080/00206814.2022.2158498

Ghorbani, Y., Nwaila, G.T., Zhang, S.E., Bourdeau, J.E., Cánovas, M., Arzua, J., Nikadat, N. 2023. Moving towards deep underground mineral resources: drivers, challenges and potential solutions: Resources Policy, v. 80, p. 103222. https://doi.org/10.1016/j.resourpol.2022.103222

Guanter, L., Kaufmann, H., Segl, K., Foerster, S., Rogass, C., Chabrillat, S., Kuester, T., Hollstein, A., Rossner, G., Chlebek, C., Straif, C., Fischer, S., Schrader, S., Storch, T., Heiden, U., Mueller, A., Bachmann, M., Mühle, H., Müller, R., Habermeyer, M., Ohndorf, A., Hill, J., Buddenbaum, H., Hostert, P., Van Der Linden, S., Leitão, P., Rabe, A., Doerffer, R., Krasemann, H., Xi, H., Mauser, W., Hank, T., Locherer, M., Rast, M., Staenz, K., Sang, B. 2015. The EnMAP spaceborne imaging spectroscopy mission for Earth observation:

Remote Sensing, v. 7, p. 8830-8857. https://doi.org/10.3390/rs70708830

Hanley, J.A., McNeil, B.J. 1982. The meaning and use of the area under a receiver operating characteristic (ROC) curve: Radiology, v. 143, p. 29-36. https://doi.org/10.1148/radiology.143.1.7063747

Harris, J.R., Sanborn-Barrie, M., Panagapko, D.A., Skulski, T., Parker, J.R. 2006. Gold prospectivity maps of the Red Lake greenstone belt: application of GIS technology: Canadian Journal of Earth Sciences, v. 43, p. 865-893. https://doi.org/10.1139/e06-020

Harris, J.R., Lafrance, B., Grunsky, E., Behnia, P., Naghizadeh, M., Lawley, C., Parsa, M. 2025. Orogenic gold mineral prospectivity mapping of the Geraldton area, Ontario: discussion of key issues: Earth Science Informatics, v. 18, p. 360. https://doi.org/10.1007/s12145-025-01831-y

Hauff, P. 2008. An overview of VIS-NIR-SWIR field spectroscopy as applied to precious metals exploration: Spectral International Inc., Arvada, Colorado, USA.

Iizumi, S., Batkhishig, B. 2000. Petrology of Carboniferous Shuteen pluton in the South Gobi fold belt, South Mongolia: Geological Society of Japan, Annual Meeting, 107th, Matsue City, Japan, p. 319.

Ince, E.S., Barthelmes, F., Reißland, S., Elger, K., Förste, C., Flechtner, F., Schuh, H. 2019. ICGEM-15 years of successful collection and distribution of global gravitational models associated services, and future plans: Earth System Science Data, v. 11, p. 647-674. https://doi.org/10.5194/essd-11-647-2019

Jahn, B., Wu, F., Chen, B. 2000. Granitoids of the Central Asian Orogenic Belt and continental growth in the Phanerozoic: Earth and Environmental Science Transactions of the Royal Society of Edinburgh, v. 91, p. 181-193. https://doi.org/10.1017/S0263593300007367

Japan International Cooperation Agency. 1992. Report on the mineral exploration in the Uudam-tal area, Mongolian People's Republic (phase 1): Japan International Cooperation Agency, Tokyo.

Josso, P., Hall, A., Williams, C., Le Bas, T., Lusty, P., Murton, B. 2023. Application of random-forest machine learning algorithm for mineral predictive mapping of Fe-Mn crusts in the World Ocean: Ore Geology Reviews, v. 162, p. 105671. https://doi.org/10.1016/j.oregeorev.2023.105671

Kokaly, R.F., Clark, R.N. 1999. Spectroscopic determination of leaf biochemistry using band-depth analysis of absorption features and stepwise multiple linear regression: Remote Sensing of Environment, v. 67, p. 267-287. https://doi.org/10.1016/S0034-4257(98)00084-4

Koldasbayeva, D., Tregubova, P., Gasanov, M., Zaytsev, A., Petrovskaia, A., Burnaev, E. 2024. Challenges in data-driven geospatial modeling for environmental research and practice: Nature Communications, v. 15, p. 10700. https://doi.org/10.1038/s41467-024-55240-8

Lamb, M.A., Cox, D. 1998. New 40Ar/39Ar age data and implications for porphyry copper deposits of Mongolia: Economic Geology, v. 93, p. 524-529. https://doi.org/10.2113/gsecongeo.93.4.524

Lowell, J.D., Guilbert, J.M. 1970. Lateral and vertical alteration-mineralization zoning in porphyry ore deposits: Economic Geology, v. 65, p. 373-408. https://doi.org/10.2113/gsecongeo.65.4.373

Mahboob, M.A., Celik, T., Genc, B. 2024. Predictive modelling of mineral prospectivity using satellite remote sensing and machine learning algorithms: Remote Sensing Applications: Society and Environment, v. 36, p. 101316. https://doi.org/10.1016/j.rsase.2024.101316

Mars, J.C., Rowan, L.C. 2011. ASTER spectral analysis and lithologic mapping of the Khanneshin carbonatite volcano, Afghanistan: Geosphere, v. 7, p. 276-289. https://doi.org/10.1130/GES00630.1

Mastop De Oliveira, J.K., Silva, A.M., Tavares, F.M., Lima Costa, I.S. 2025. Mapping Cu-Au mineral potential (IOCG and Cu-Au polymetallic) in the Northern Copper Belt, Carajás Mineral Province: a data-driven, mineral systems-based approach: Ore Geology Reviews, v. 185, p. 106770. https://doi.org/10.1016/j.oregeorev.2025.106770

Mokhtari, A.R., Behnia, P., Lafrance, B., Naghizadeh, M., Simmons, J.M., Harris, J.R. 2025. Mineral prospectivity mapping of orogenic gold mineralization in the Malartic-Val-d'Or Transect area, Metal Earth project,

Canada: Ore Geology Reviews, v. 178, p. 106498. https://doi.org/10.1016/j.oregeorev.2025.106498

Munkhtsengel, B., Chimedtseren, A., Javkhlan, O., Batkhishig, B., Altanzul, B., Soyolmaa, B., Burenjargal, O., Undarmaa, B, Ariuntsetseg, G., Manzshir, B., Munkh, J., Gerel, O., Tumurtogoo, O. 2018. Geology, magmatism, and mineralization of the paleo-subduction zones. Report of the Mongolian Foundation for Science and Technology Project No.ShUTT_012/2015, p. 450.

Neal, L.C., Wilkinson, J.J., Mason, P.J., Chang, Z. 2018. Spectral characteristics of propylitic alteration minerals as a vectoring tool for porphyry copper deposits: Journal of Geochemical Exploration, v. 184, p. 179-198. https://doi.org/10.1016/j.gexplo.2017.10.019

Nyamaa, B., Amarjargal, A., Bat-Uils, B., Orgil, D., Sunjidmaa, M., Munkhnasan, Ts., Nasanbat, N., Otgonjargal, Ch. 2013. Final report of the "UGZ-200 South Mongolia-VI" project on the compilation of the 1:200,000-scale geological integrated map of Mongolia (sheets L-48-XVII, XIX-XXXVI): Report No. 7390, Geological Information Center, Ulaanbaatar (in Mongolian).

Okada, K. 2022. Breakthrough technologies for mineral exploration: Mineral Economics, v. 35, p. 429-454. https://doi.org/10.1007/s13563-022-00317-3

Phillips, G.N., Vearncombe, J.R., Clemens, J.D., Day, A., Kisters, A.F.M., Von Der Heyden, B.P. 2023. Formation of Cu-Au porphyry deposits: hydraulic quartz veins, magmatic processes and constraints from chlorine: Australian Journal of Earth Sciences, v. 70, p. 1010-1033. https://doi.org/10.1080/08120099.2023.2237105

Ponomarenko, T., Nevskaya, M., Jonek-Kowalska, I. 2021. Mineral resource depletion assessment: alternatives, problems, results: Sustainability, v. 13, p. 862. https://doi.org/10.3390/su13020862

Porwal, A.K., Kreuzer, O.P. 2010. Introduction to the special issue: mineral prospectivity analysis and quantitative resource estimation: Ore Geology Reviews, v. 38, p. 121-127. https://doi.org/10.1016/j.oregeorev.2010.06.002

Rodriguez-Galiano, V., Sanchez-Castillo, M., Chica-Olmo, M., Chica-Rivas, M. 2015. Machine learning predictive models for mineral prospectivity: an evaluation of neural networks, random forest, regression trees and support vector machines: Ore Geology Reviews, v. 71, p. 804-818. https://doi.org/10.1016/j.oregeorev.2015.01.001

Rowan, L.C., Mars, J.C. 2003. Lithologic mapping in the Mountain Pass, California area using Advanced Spaceborne Thermal Emission and Reflection Radiometer (ASTER) data: Remote Sensing of Environment, v. 84, p. 350-366. https://doi.org/10.1016/S0034-4257(02)00127-X

Şengör, A.M.C., Natal'in, B.A., Burtman, V.S. 1993. Evolution of the Altaid tectonic collage and Palaeozoic crustal growth in Eurasia: Nature, v. 364, p. 299-307. https://doi.org/10.1038/364299a0

Shebl, A., Abdellatif, M., Abriha, D., Dawoud, M., Hussein Ali, M.A., Mahmoud, A.S., Kristály, F., Csámer, Á. 2025. EnMAP hyperspectral data in geological investigations: evaluation for lithological and hydrothermal alteration mapping in Neoproterozoic rocks: Gondwana Research, v. 143, p. 91-124. https://doi.org/10.1016/j.gr.2025.03.014

Sillitoe, R.H. 2010. Porphyry copper systems: Economic Geology, v. 105, p. 3-41. https://doi.org/10.2113/gsecongeo.105.1.3

Son, Y.-S., Kang, M.-K., Yoon, W.-J. 2014. Lithological and mineralogical survey of the Oyu Tolgoi region, Southeastern Gobi, Mongolia using ASTER reflectance and emissivity data: International Journal of Applied Earth Observation and Geoinformation, v. 26, p. 205-216. https://doi.org/10.1016/j.jag.2013.07.004

Son, Y.-S., Kim, K.-E., Yoon, W.-J., Cho, S.-J. 2019. Regional mineral mapping of island arc terranes in southeastern Mongolia using multi-spectral remote sensing data: Ore Geology Reviews, v. 113, p. 103106. https://doi.org/10.1016/j.oregeorev.2019.103106

Sun, W., Wang, J., Zhang, L., Zhang, C., Li, H., Ling, M., Ding, X., Li, C., Liang, H. 2017. The formation of porphyry copper deposits: Acta Geochimica, v. 36, p. 9-15. https://doi.org/10.1007/s11631-016-0132-4

Sun, T., Li, H., Wu, K., Chen, F., Zhu, Z., Hu, Z. 2020. Data-driven predictive modelling of mineral prospectivity using machine learning

and deep learning methods: a case study from southern Jiangxi Province, China: Minerals, v. 10, p. 102. https://doi.org/10.3390/min10020102

Sun, K., Chen, Y., Geng, G., Lu, Z., Zhang, W., Song, Z., Guan, J., Zhao, Y., Zhang, Z. 2024. A review of mineral prospectivity mapping using deep learning: Minerals, v. 14, p. 1021. https://doi.org/10.3390/min14101021

Tungalag, N., Jargalan, S., Khashgerel, B.-E., Mijiddorj, C., Kavalieris, I. 2019. Characteristics of the Late Devonian Tsagaan Suvarga Cu-Mo deposit, southern Mongolia: Mineralium Deposita, v. 54, p. 369-380. https://doi.org/10.1007/s00126-018-0812-6

van der Meer, F.D., van der Werff, H.M.A., van Ruitenbeek, F.J.A. 2014. Potential of ESA's Sentinel-2 for geological applications: Remote Sensing of Environment, v. 148, p. 124-133. https://doi.org/10.1016/j.rse.2014.03.022

van der Werff, H.M.A., van der Meer, F.D. 2016. Sentinel-2A MSI and Landsat 8 OLI provide data continuity for geological remote sensing: Remote Sensing, v. 8, p. 883. https://doi.org/10.3390/rs8110883

Wainwright, A.J., Tosdal, R.M., Wooden, J.L., Mazdab, F.K., Friedman, R.M. 2011. U-Pb (zircon) and geochemical constraints on the age, origin, and evolution of Paleozoic arc magmas in the Oyu Tolgoi porphyry Cu-Au district, southern Mongolia: Gondwana Research, v. 19, p. 764-787. https://doi.org/10.1016/j.gr.2010.11.012

Weiss, A.D. 2001. Topographic position and landforms analysis. Presented at the ESRI Users Conference, San Diego, CA.

Windley, B.F., Alexeiev, D., Xiao, W., Kröner, A., Badarch, G. 2007. Tectonic models for accretion of the Central Asian Orogenic Belt: Journal of the Geological Society, v. 164, p. 31-47. https://doi.org/10.1144/0016-76492006-022

Xiao, W., Windley, B.F., Han, C., Liu, W., Wan, B., Zhang, J., Ao, S., Zhang, Z., Song, D. 2018. Late Paleozoic to early Triassic multiple roll-back and oroclinal bending of the Mongolia collage in Central Asia: Earth-Science Reviews, v. 186, p. 94-128. https://doi.org/10.1016/j.earscirev.2017.09.020

Yang, F., Zuo, R., Kreuzer, O.P. 2024. Artificial intelligence for mineral exploration: a review and perspectives on future directions from data science: Earth-Science Reviews, v. 258, p. 104941. https://doi.org/10.1016/j.earscirev.2024.104941

Youden, W.J. 1950. Index for rating diagnostic tests: Cancer, v. 3, p. 32-35. https://doi.org/10.1002/1097-0142(1950)3:1<32::AID-CNCR2820030106>3.0.CO;2-3

Zuo, R., Carranza, E.J.M. 2011. Support vector machine: a tool for mapping mineral prospectivity: Computers & Geosciences, v. 37, p. 1967-1975. https://doi.org/10.1016/j.cageo.2010.09.014